Automatic, Localized *in Vivo* Adjustment of All First- and Second-Order Shim Coils

Rolf Gruetter

The implementation of a "fast, automatic shimming technique by mapping along projections" (FASTMAP) on a 2.1-Tesla whole-body system is described. The method provides a localized adjustment of all first- (X, Y, Z) and second-order (Z^2, ZX, ZY, X^2-Y^2, 2XY) coils in 2 min. The time savings are achieved by mapping the magnetic field along six projections rather than from whole-imaging data sets. An analysis of noise error propagation suggests that in 64-ml volumes the residual linewidths obtained with the method are negligible when the signal-to-rms-noise ratio is above 30. The initial application of the method to localized ^{13}C, ^{31}P, and ^{1}H spectroscopy of the human brain resulted in linewidths of ~2 Hz for ^{13}C (144-ml volume), ~2.5 Hz for ^{31}P (36-ml volume) and ~4 Hz for ^{1}H (36-ml volume) with symmetric and reproducible lineshapes.

Key words: automatic shimming; magnetic field mapping; homogeneity adjustment; *in vivo*.

INTRODUCTION

The quality of *in vivo* magnetic resonance spectroscopy, spectroscopic imaging (1), and to a lesser extent imaging modalities such as chemical shift selective methods for fat-water suppression (2) or T_2^*-weighted high-field echo-planar imaging (3) depend on a spatially homogeneous magnetic field over the region of interest. For *in vivo* spectroscopy, a homogeneity on the order of 0.01–0.1 ppm is required, which introduces the additional time consuming shim adjustment procedure into the setup. Shimming can be a very time-consuming process, especially when performed iteratively, which may depend on operator skills as well as the starting conditions (4). Clearly, such a situation is undesirable in the context of minimizing time requirements for human applications.

Most localized shimming techniques have been restricted to the adjustment of the linear coils X, Y, and Z (5, 6) using primarily the iterating maximization of the envelope of the time-domain signal. The exclusive use of these three coils had a deeper cause in the fact that away from the magnet center, adjustment of higher-order shim coils will interfere with that of lower-order coils, which may result in impractical procedures (7).

MRM 29:804–811 (1993)

From the Department of Molecular Biology and Biochemistry, Yale University, New Haven, Connecticut.

Address correspondence to: Rolf Gruetter, Magnetic Resonance Center, University and Inselspital Bern, Inselheimmatte, CH-3010 Bern, Switzerland.

A preliminary account of part of this work was presented at the 10th Annual Meeting, Soc. Magn. Reson. Med., p. 468, San Francisco, August 10–16 (1991)

Received August 7, 1992; revised December 14, 1992; accepted December 14, 1992.

0740-3194/93 $3.00

Recently, several automatic shimming techniques capable of circumventing this problem have been described (8–13). Some of these techniques rely on the acquisition of chemical shift images (8, 9) whereas others use phase difference images (10–12). However, based on arguments of shim coil design, Gruetter and Boesch (13) have shown that it is not necessary to acquire the data in images, but the magnetic field measurement acquired along a few linear projections is sufficient to characterize the magnetic field in terms of spherical harmonic functions. The design of shim coils is generally such that the field generated by a shim coil is essentially described by one spherical harmonic function. The measured coefficients of spherical harmonic terms in the field expansion are thus directly proportional to the shim correction currents, which results in considerable time savings.

This paper describes the implementation of a "fast automatic shimming technique by mapping along projections" (FASTMAP), that adjusts all eight first- and second-order shim coils locally. The initial application to ^{31}P, ^{13}C, and ^{1}H MRS of the human brain is reviewed and examples of the spectral resolution that can be achieved at 2.1 T with this method are shown. A calculation of the effect of noise error propagation into the adjustment is included. The proposed technique is discussed and compared with other automatic shimming techniques that have been recently described.

METHODS

Review of Theory

The magnetic field can be written in the form (14)

$$B(r,\theta,\phi) = \sum_n (r^n * \sum_i (k_{ni} * W_{ni}(\phi,\theta))), \qquad [1]$$

where r = 0 in this notation can be at any point (x_0, y_0, z_0) in the magnet. The angular functions $W_{ni}(\phi,\theta)$ are given in Table 1 for all first- and second-order coils. Along a straight line that runs through r = 0, denoted by the superscript $^{(j)}$, the field variation is a polynomial of the form $a_0^{(j)} + a_1^{(j)}r + a_2^{(j)}r^2 + \ldots$, since the $W_{ni}(\phi^{(j)},\theta^{(j)})$ are constant. Gruetter and Boesch (13) have shown that all first- and second-order shim terms can be unequivocally determined from the field measurement along the six projections that are parallel to the side diagonals of the cube. The coefficients k_{ni} of the expansion can then be computed according to Eq. [2] (13)

$$k_{ni} = \frac{\sum_j a_n^{(j)} * W_{ni}(\phi^{(j)},\theta^{(j)})}{\sum_j W_{ni}(\phi^{(j)},\theta^{(j)})^2}, \qquad [2]$$

Table 1
First- and Second-Order Shim Coils, the Calculated Coefficients, and Calibration

Shim name	Associated function $r^nW_{ni}(\theta,\phi)$	Coefficients[a] k_{ni} (ppm/cm^n)	Calibration of shim currents[b]	
			(ppm/cm^n)	Unwanted (10^{-2}ppm/cm)[c]
X	$r\sin\theta\cos\phi$	$k_{11}=(a_1{}^{xy}-a_1{}^{yx}+a_1{}^{xz}-a_1{}^{zx})*8^{-1/2}$	$0.461rW_{11}$	
Y	$r\sin\theta\sin\phi$	$k_{12}=(-a_1{}^{xy}-a_1{}^{yx}+a_1{}^{yz}-a_1{}^{zy})*8^{-1/2}$	$0.459rW_{12}$	
Z	$r\cos\theta$	$k_{13}=(a_1{}^{xz}+a_1{}^{zx}+a_1{}^{yz}+a_1{}^{zy})*8^{-1/2}$	$0.484rW_{13}$	
Z^2	$r^2(3\cos^2\theta-1)/2$	$k_{21}=(-2*a_2{}^{xy}-2*a_2{}^{yx}+a_2{}^{xz}+a_2{}^{zx}+a_2{}^{yz}+a_2{}^{zy})/3$	$-0.0660r^2W_{21}$	$0.64rW_{11}-1.12rW_{13}$
ZX	$r^2\sin\theta\cos\theta\cos\phi$	$k_{22}=a_2{}^{xz}-a_2{}^{zx}$	$+0.0112r^2W_{22}$	$0.34rW_{11}$
ZY	$r^2\sin\theta\cos\theta\sin\phi$	$k_{23}=a_2{}^{yz}-a_2{}^{zy}$	$-0.0113r^2W_{23}$	$0.31rW_{12}$
X^2-Y^2	$r^2\sin^2\theta\cos2\phi$	$k_{24}=(a_2{}^{xz}+a_2{}^{zx}-a_2{}^{yz}-a_2{}^{zy})/2$	$+0.0111r^2W_{24}$	$0.16rW_{11}-0.15rW_{12}$
2XY	$r^2\sin^2\theta\sin2\phi$	$k_{25}=(-a_2{}^{xy}+a_2{}^{yx})/2$	$+0.0112r^2W_{25}$	$-0.39rW_{11}+0.21rW_{12}$

[a] The orientations of the projections $^{(j)}$ were given by the pairs $(\theta^{(j)}, \phi^{(j)})$, i.e. ^{xy}=(90°,−45°), ^{yx}=(90°,−135°), ^{zx}=(45°,0°), ^{xz}=(45°,180°), ^{zy}=(45°,−90°), ^{yz}=(45°,90°).
[b] Given are the calibration constants (multiplied by r^nW_{ni}) when the SCM setting is changed by 1000, which in most cases corresponded to a 1-amp change in coil current.
[c] Field generated by shim coils other than the associated spherical harmonic. Terms below $0.07\cdot10^{-2}$ ppm/cm were omitted.

which results in the equations given in column 3 of Table 1 for the k_{ni}. The $a_n{}^{(j)}$ represent the polynomial coefficients that are measured along the projections indicated in footnote a at the bottom of Table 1.

Pulse Sequence

The stimulated echo sequence in Fig. 1 was implemented. To reduce the time required for pulse gain adjustments, the sequence uses three identical sinc pulses defined over $\pm\pi$ of 2.5-ms duration with 1.5-kHz bandwidth. The x′ and z′ gradient strength was set to 2 kHz/cm resulting in 7.5-mm thick bars, whose position was defined from the frequency of the second and third pulses and the orientation by the direction of the orthogonal x′ and z′ gradients. The read gradient (denoted y′ in Fig. 1) was set to a strength of 1 kHz/cm, i.e., 2.4 mT/m. The frequency of the first pulse was set to that of water, whereas the frequency f during readout was set such that f = 0 corresponded to the volume center, defined as r = 0. Frequency lists were calculated with a Pascal program based on the user-provided coordinates (x_0, y_0, z_0) of the volume center. Sweep width was 25 kHz with 256 complex points resulting in a nominal resolution of Δr = 0.1 cm/point along the bar. The echo time TE was 23 ms and TM was 9 ms. The repetition time TR was 1.7 s during which eddy-current effects have died away to a negligible level, as verified by obtaining identical results with a prolonged TR of 10 s. Applying the first pulse of the stimulated echo sequence without gradients ensured that the field measurement was not influenced by eddy-current effects from within the sequence.

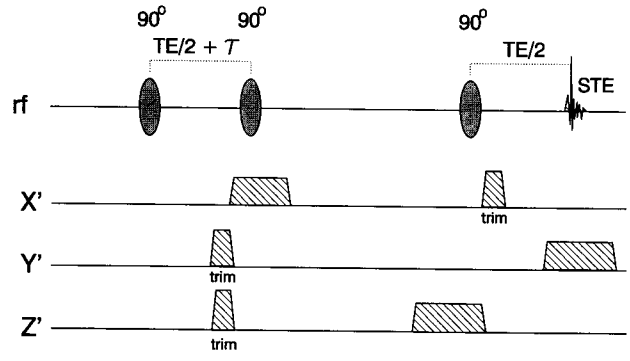

FIG. 1. Pulse sequence used to select signal along bars. The second and third pulse select the signal along a bar. The first pulse is applied in the absence of gradients resulting in a phase evolution during τ in the first echo delay (between pulse 1 and 2) that is completely independent of eddy-current effects. The phase difference of projections obtained with and without τ is used to calculate the field. The slice gradients (x′ and z′) form together with the read (y′) gradient an orthogonal system. The gradient orientations are created by linear combinations of the magnet gradients x, y, and z according to the orientations given in footnote a of Table 1.

Implemented Procedure (Fig. 2)

The pulse sequence (Fig. 1) was applied without dummy scans in all six directions consecutively, and then, to encode the magnetic field information, repeated along

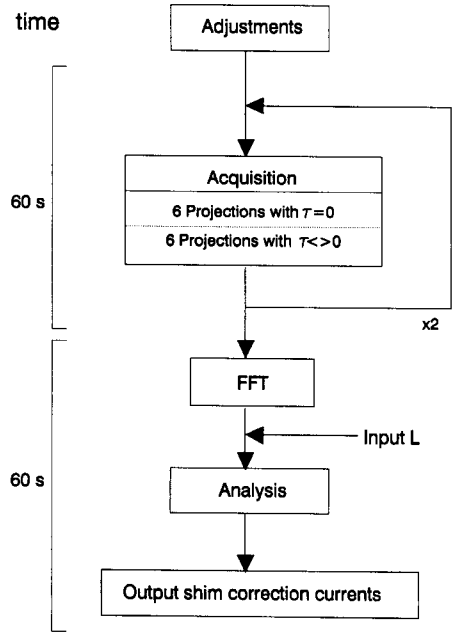

FIG. 2. Flow diagram of implemented shim procedure.

the six orientations, with the first TE/2 period incremented by τ. This resulted in 12 acquisitions that were stored in different memory blocks. The minimal time needed to measure the field information was therefore 20 s. The sequence was repeated once for phase cycling resulting in a total experimental time of below 1 min. The echoes were then sensitivity enhanced by Gaussian multiplication, Fourier transformed and the resulting 12 projections written to a disk file for analysis. Upon user input of the desired bar length L, the phase differences of projections acquired with the extra delay τ, $z_{2i}^{(j)}$, to those acquired without, $z_{1i}^{(j)}$, were calculated within $\pm L/2$ in each projection using the *complex* division (10) of the corresponding projections acquired with $\tau = 0$ and $\neq 0$, i.e.,

$$\Delta\varphi_i^{(j)} = \arg(z_{2i}^{(j)}/z_{1i}^{(j)}). \quad [3]$$

This simplified the calculations tremendously compared with the difference of the separately calculated phases $\varphi_{2i}^{(j)} = \arg(z_{2i}^{(j)})$ and $\varphi_{1i}^{(j)} = \arg(z_{1i}^{(j)})$. Phase discontinuities along the calculated phase differences $\Delta\varphi_i^{(j)}$ were eliminated by testing for π phase jumps and by adding the same multiple of π between two consecutive discontinuities, assuming the phase noise to be well below $\pi/6$ rad. The phase variation between digitized points was thus required to be less than $5\pi/6$ rad/mm. The frequency (expressed in ppm) was calculated as

$$\Delta\nu_i^{(j)} = \frac{1}{\nu_0}\frac{1}{2\pi\tau}\Delta\varphi_i^{(j)}, \quad [4]$$

where ν_0 is the Hz-to-ppm conversion factor, which is 89.43 Hz/ppm at 2.1T. τ is the phase encoding delay, that is the time by which the first TE/2 period in Fig. 1 is increased. The scaling (Eq. [4]) was applied after the polynomial regression to minimize computational efforts. Second-order polynomials of the form

$$a_0^{(j)} + a_1^{(j)}r + a_2^{(j)}r^2 \quad [5]$$

were used as the model function for $\Delta\nu_i^{(j)}$ utilizing explicit formulas that are given in the Appendix. Since Eq. [3] does not allow for absolute phase determination, the constant term $a_0^{(j)}$ was fitted individually for each projection $^{(j)}$. From the *measured* $a_1^{(j)}$ and $a_2^{(j)}$ the coefficients k_{ni} of the spherical harmonics are calculated according to the expressions in column 3 of Table 1.

Calibration of shim currents was performed by successively changing the shim current monitor (SCM) setting of one coil at seven values centered about the optimal setting and by measuring the k_{ni} at the magnet center (x_0, y_0, z_0) = (0, 0, 0) as a function of the SCM setting. The results for the present implementation are given in the fourth column of Table 1, with most shim coils being well described by their theoretical field function. The fifth column in Table 1 shows that some of the second-order coils produced small linear terms. These slight imperfections were eliminated by changing the first-order coils according to the change in second-order coils, which was easily incorporated into the present procedure. For instance, changing the SCM setting of the ZX shim coil by +1000 results in a small x gradient of +0.0034 ppm/cm (Table 1) that was cancelled by changing the SCM setting of the x coil by −1000*(0.0034/0.461) = −7 units. This procedure is very similar to the matrixing frequently used on high-resolution spectrometers such as the concurrent alteration of the Z^0 shim current according to the changes in Z^2 and Z^4 coil currents.

The effect of displacement can be explicitly calculated from the conversion of the spatial functions $W_{ni}(\theta, \phi)$ into Cartesian coordinates (13). Assuming the changes in second-order coils, denoted by k_{2i}, to cancel the measured inhomogeneities at the position x_0, y_0, z_0, they produce the linear terms k_{1i}^*,

$$\begin{aligned} k_{11}^* &= -k_{21}^*x_0 \quad +k_{22}^*z_0 \quad\quad +k_{24}^*2^*x_0 \; +k_{25}^*2^*y_0 \\ k_{12}^* &= -k_{21}^*y_0 \quad\quad +k_{23}^*z_0 \; -k_{24}^*2^*y_0 \; +k_{25}^*2^*x_0 \\ k_{13}^* &= +k_{21}^*2^*z_0 \; +k_{22}^*x_0 \; +k_{23}^*y_0 \end{aligned} \quad [6]$$

The terms k_{1i}· calculated in Eq. [6] have to be subtracted from the linear terms k_{1i} that correct for the measured inhomogeneity. Alternatively, the sequence can be run along the three magnet axes as described in (13) to correct for these additional linear terms.

A shift in the voxel center frequency may arise due to the position being away from the isocenter, which can be explicitly calculated, or adjusted via the spectrometer frequency or the Z^0 shim coil, respectively, to ensure accurate volume localization.

Experimental

All experiments were carried out on a 2.1-T Bruker-Biospec whole-body magnet (Oxford Research Systems-Bruker, Billerica, MA) equipped with either a 75-cm unshielded or a 72-cm diameter active-shielded gradient set (Oxford Magnet Technology, Oxford, UK). The system was equipped with the following higher-order resistive shim coils: Z^2, X^2-Y^2, 2XY, ZX, ZY, Z^3, Z^2Y, Z^2X, and Z^4 controlled via the shim control monitor (SCM) unit, and a gradient preemphasis as well as a Z^0 compensation unit. The spectrometer was equipped with an ASPECT 3000 computer and operated with DISNMR software (DISR88). Computer programs on the spectrometer computer (including the output to the SCM unit) were written in Pascal (Pascom, version 1986). Numerical simulations were performed on a Zenith 16–386SX 16-MHz desktop computer equipped with a 387SX math coprocessor using Turbo Pascal 6.0 (Borland).

RESULTS

The procedure is summarized in Fig. 2. After pulse gain and receiver gain adjustments, the constant field term Z^0 was set to zero by adjusting the water frequency offset measured with an unsuppressed stimulated-echo sequence (TE = 23 ms) obtained from a $1.5 \times 1.5 \times 1.5 cm^3$ volume at the position (x_0, y_0, z_0). The six projections indicated in footnote a in Table 1 were acquired using the pulse sequence in Fig. 1 as described above. For brain studies, τ in Fig. 1 was typically between 30 and 50 ms. The data acquisition was repeated once, resulting in an experimental time of below 1 min. The 12 memory blocks

were stored on disk after Fourier transformation and analyzed on the spectrometer computer by a Pascal program. After the input of the bar length L, phase differences were calculated within ±L/2 according to Eq. [3]. Polynomial regression yielded the $a_1^{(j)}$ and $a_2^{(j)}$, from which the k_{ni} and corresponding shim current changes were calculated according to the expressions in column 3 and 4 of Table 1 and the linear terms were corrected for the volume position according to Eq. [6]. The corresponding change in shim currents were then output to the SCM unit within the same Pascal program. The time needed for the whole calculations including FFT was 1 min., resulting in a total adjustment time of less than 2 min. The subsequent fine adjustment of the center frequency had to be delayed because of a large transient B_0 shift with a time constant of the order of a minute. This shift was shown to be induced in the magnet by the abrupt change in the Z^2 coil current. The time required to stabilize was reduced somewhat by emulating an overshoot of the Z^2 coil by hand similar to eddy-current compensation schemes.

The sequence was extensively tested in phantoms. A full width at half height of 0.015 ppm was achieved on a 10-cm diameter sphere filled with water, as well as on a 20-cm sphere. The linewidth for a 1.5^3-ml volume was ~0.003 ppm in aqueous phantoms.

Noise Error Propagation

In the absence of noise in the projections and when higher-order inhomogeneities (n ≥ 3) are insignificant, the FASTMAP method renders a perfect homogeneity. However, projections are acquired in the presence of noise, which will produce a suboptimal adjustment. This section considers the effects due to limited signal-to-noise, which provides insight into the optimal operating conditions for the FASTMAP technique. Eq. [7] below applies to all techniques that are based on phase difference calculations.

The calculations are illustrated in the Appendix. Throughout this section, a spatially homogeneous signal distribution shall be assumed and the noise in the real or imaginary part of the projections is assumed to be uncorrelated and of Gaussian distribution with the rms amplitude σ.

The rms error of the frequency $\Delta\nu$ (Eq. [4]) is given by:

$$\sigma_{ppm} = \frac{1}{\nu_0}\frac{1}{2\pi T_2^*}\frac{(1+e^{2x})^{1/2}}{x}\frac{1}{M/\sigma}. \qquad [7]$$

In Eq. [7], M/σ is the signal-to-rms-noise ratio in the projection obtained without the extra-delay τ (Fig. 1), $e^{-\tau/T_2^*}$ represents the factor by which the projections obtained with the extra-delay are attenuated, and $x \equiv \tau/T_2^*$. The function f(x) in Eq. [7] is plotted in Fig. 3. It has a minimum value of 2.9 at x = 1.11 and is flat over a relatively large range of x values. For instance, f(x) is only 10% above its minimum value in the range of $\tau = 0.7T_2^*$ to $1.6T_2^*$ and is less than twice the minimum in the range of $\tau = 0.3T_2^*$ to $2.8T_2^*$. Note that neglecting the effect of signal decay during the extra delay τ, i.e., assuming infinite T_2^*, results in $f(x) = 2^{1/2}/x$, making Eq. [7] essentially identical to the expression given in Ref. 12.

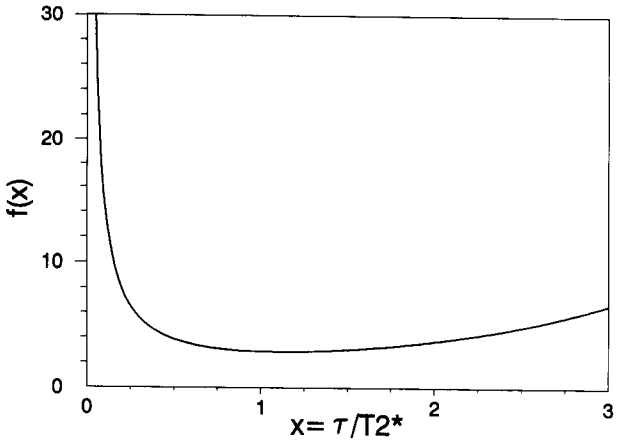

FIG. 3. Noise error propagation. Shown is the function $f(x) = (1+e^{2x})^{1/2}/x$ as a function of $x = \tau/T_2^*$ used in Eq. [7].

The subsequent propagation of the noise error in the frequency calculation into the calculation of the polynomial coefficients a_1 and a_2 can be explicitly calculated. The rms amplitude of the noise error for a_1 and a_2 is given by σ_1 and σ_2, respectively (see Appendix):

$$\sigma_1 = \sigma_{ppm} * L^{-3/2} * \Delta r^{1/2} * C_1$$
$$\sigma_2 = \sigma_{ppm} * L^{-5/2} * \Delta r^{1/2} * C_2. \qquad [8]$$

L is the bar length (in cm) over which the polynomial regression was performed, Δr the digital resolution in cm/point. The constants are $C_1 = 2*3^{1/2}$ and $C_2 = 6*5^{1/2}$. The expressions in Eq. [8] were verified by numerical Monte-Carlo simulations at variable L (23).

The noise present in the projections will result in an imperfect adjustment, i.e., in a finite full width at half height ($FWHH_{ppm}$) of the frequency distribution in the measured volume. Figure 4 shows $FWHH_{ppm}$ as a func-

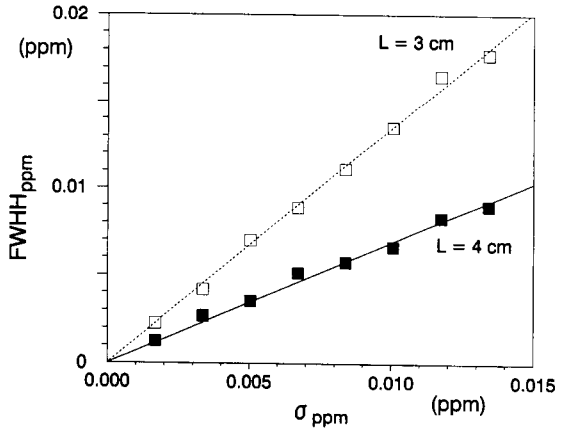

FIG. 4. Effect of finite signal-to-noise on the final homogeneity. The ordinate represents σ_{ppm} (Eq. [7]), the abscissa the average full width at half height ($FWHH_{ppm}$), in ppm, of the resulting field distribution in a cubic 4 × 4 × 4 cm^3 volume. Bar length L was 4 cm (solid squares) and L = 3 cm (open squares). The solid and the dashed lines were obtained by linear regression (y = ax). Each point represents the average of 100 Monte-Carlo trials using Gaussian deviates (23) with the rms amplitude σ_{ppm} in the phase calculated along six bars of length L.

tion of σ_{ppm} for a 4 × 4 × 4 cm^3 cubic volume calculated for a bar length of 3 cm and 4 cm, respectively. In an aqueous phantom measured in a resonator (90° pulse width was 350 μs at 500-W power), σ_1 = $0.041 \cdot 10^{-2}$ppm/cm and σ_2 = $0.024 \cdot 10^{-2}$ppm/cm^2 were measured using the pulse sequence with τ = 30 ms and L = 4 cm. According to Eq. [8] this corresponds to the leftmost point in Fig. 4 (L = 4 cm). Note, that the average $FWHH_{ppm}$ of the curve is directly proportional to the length of the side of the cubic volume, e.g., for a 2 × 2 × 2 ml volume the vertical scale in Fig. 4 has to be divided by 2.

As an example, assuming a T_2^* of 70 ms, which is close to the value for grey matter (see below), and assuming $\tau >$ 20 ms, σ_{ppm} is calculated from Eq. [7] to be below $0.15*(M/\sigma)^{-1}$, which translates into a σ_{ppm} of less than 0.005 ppm for a M/σ of 30. For an L of 4 cm and the Δr = 0.1 cm/point used in the present implementation, an average achieved linewidth of the field distribution, $FWHH_{ppm}$, of ~0.004 ppm for the 64-ml volume is achieved according to Fig. 4.

In Vivo Spectroscopy of Human Brain

The method has been used to obtain localized spectra from the occipital lobe of the human brain using mostly surface coils (15–19). τ in Fig. 1 was typically between 30 and 50 ms and L was in most cases between 3 and 5 cm, which posed no problem even when using surface coils as small as 6 cm in diameter. Typical correction terms were as high as ~0.1 ppm/cm for the linear coils and ~0.01 ppm/cm^2 for the quadratic coils. The linewidth of the water resonance in grey matter was approximately 0.05 ppm in 1.5^3 cm^3 volumes, corresponding to a T_2^* of ~70 ms.

Figure 5 shows a ^{31}P spectrum obtained from a 36-ml volume encompassing the visual cortex. Contributions of heteronuclear coupling to the linewidths were eliminated using WALTZ-16 ^1H decoupling similar to previous studies (20). The localization sequence was ISIS (21) used as in Ref. 16, but without NOE generation. The native linewidth of phosphocreatine (PCr) was ~2.5 Hz, corresponding to ~0.0075 ppm.

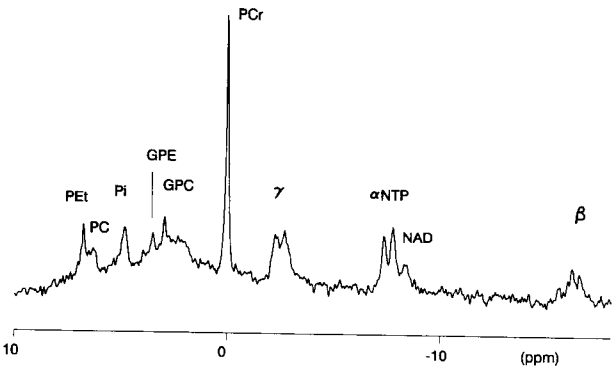

FIG. 5. Localized ^{31}P NMR of the human brain. The spectrum was obtained with WALTZ-16 decoupling to remove the contributions of heteronuclear coupling to the linewidths. Processing consisted of 2-Hz exponential multiplication. Acquisition time was 205 ms, repetition time 3 s. Localization was based on ISIS performed as described previously (15), but without NOE generation and an 8-cm (^{31}P) with a concentric 14-cm diameter coil (^1H) was used. (PE = phosphorylethanolamine, PC = phosphorylcholine, and other phosphomonoester compounds, GPE = glycerophosphorylethanolamine, GPC = glycerophosphorylcholine, PCr = phosphocreatine, NTP = nucleotide triphosphate, NAD = $NAD(P)^+$/NAD(P)H, and other dinucleotides.)

In vivo ^1H spectroscopy of 36-ml volumes close to the brain surface benefitted from the improved homogeneity, which resulted in a stable and reproducible water suppression with concomitant improvements in baseline stability (22). ^1H NMR spectroscopy was used with the proposed shim technique to observe the glucose signal in ^1H difference spectra (17) and to detect the αH1 resonance at 5.23 ppm (19). Linewidths and lineshapes were highly reproducible. Linewidths of NAA and Cr were typically ~4 Hz, i.e., ~0.04 ppm for this relatively large volume close to the surface of the brain. As an illustration of these studies (17, 19, 22), Fig. 6 shows ^1H spectra obtained from 36-ml volumes in the occipital lobe as a spin echo using a semiselective θ_x-t-θ_{-x} refocusing pulse using the pulse sequence previously described in detail in Ref. 17. Figure 6A shows a spectrum with the excitation maximum set to the amino acid region (t = 2.5 ms, echo time TE = 13 ms) and in (B) the maximum has been set to inositol (t = 5 ms, TE = 16 ms). *In vivo* lineshapes were close to Lorentzian, as illustrated in Fig. 6C by the similarity with phantom spectra containing glutamate, glutamine, and N-acetyl-aspartate. The difference between *in vivo* and solution spectra was almost at the noise level between 2.0 and 2.7 ppm (Fig. 6C, bottom).

The present shim technique has improved the resolution ^{13}C NMR spectroscopy of the human brain (15, 16, 18), which has been used for the detection of *natural abundance* signals from metabolites in the human brain such as *myo*-inositol and N-acetyl-aspartate (16), for the quantitative measurement of glucose in the human brain (15), and for the detection of narrow amino acid resonances after [1-^{13}C] glucose infusions (18). For instance, the C2, C3, and C4 resonances of labeled glutamate were resolved from those of glutamine as illustrated in Fig. 7, which is from Ref. 18. Linewidths were below 0.1 ppm, i.e., 2 Hz, allowing the separation of the C2 of Glu from C2 of Gln, which are separated by 0.5 ppm.

DISCUSSION

The implementation of a completely automatic *localized* shimming method, "fast automatic shimming technique by mapping along projections" (FASTMAP), on a 2.1-Tesla whole-body system is described that allows the adjustment of all linear (X, Y, Z) and quadratic (Z^2, X^2-Y^2, ZX, ZY, 2XY) shim coils within 2 min. Considering the high spectral resolution and quality that can be achieved as illustrated Refs. 15–19 (Figs. 5–7), this represents a marginal time requirement for human applications. The method can be implemented on any system capable of standard imaging methods, even when severe eddy-current effects persist, since the phase evolution during the extra-delay τ in Fig. 1 is unaffected by eddy-currents.

The linewidth of 2.5 Hz measured for PCr in 36 ml

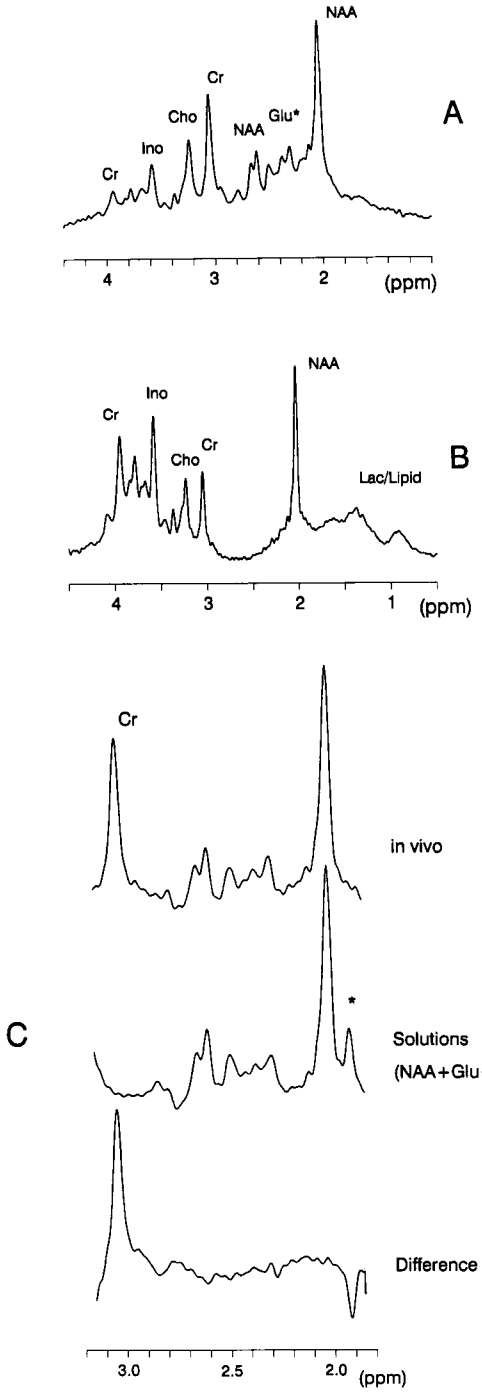

FIG. 6. Localized short-echo ^{1}H NMR spectra of the human brain. The spectra were obtained from 36-ml volumes in the occipital lobe as a spin echo with a semiselective θ_x-t-θ_{-x} refocusing pulse. The excitation maximum was set in (A) to 2.5 ppm (t = 2.5 ms, TE = 13 ms) and in (B) to inositol (t = 5 ms, TE = 16 ms). The *in vivo* spectral region (t = 2.5 ms, TE = 26 ms) from 1.85 to 3.15 ppm is shown in (C) at the top and the middle is a linear combination of corresponding linebroadened phantom spectra containing glutamate (Glu), glutamine (Gln), or N-acetyl-aspartate (NAA). The phantom spectra were obtained from separate 2l bottles preheated to 37°C containing 50 mM solutions (pH = 7.1) of the respective metabolite plus 10 mM acetate, denoted by *. All *in vivo* spectra were zero-filled and are shown without linebroadening. Acquisition time was 256 ms, and TR = 2.5 s. Localization was based on ISIS with outer volume suppression, described previously (17, 19). (Cr = creatine + phosphocreatine; Glu* = glutamate + glutamine; Ino = inositol + glycine; Cho = trimethylamine resonances; NAA = N-acetyl-aspartate).

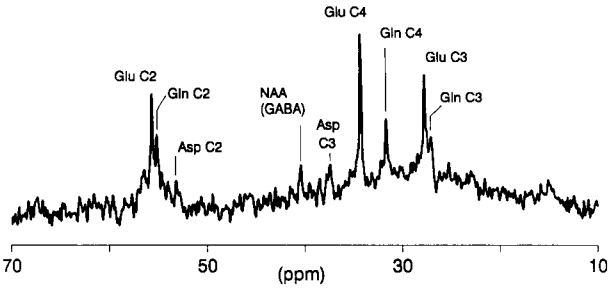

FIG. 7. Example of localized ^{13}C NMR of the human brain. Shown is a localized ^{13}C NMR spectrum from Ref. 18, obtained from a 144-ml volume in the occipital lobe after several hours of [1-^{13}C] glucose infusion. Localization was based on ISIS (15). Processing consisted of exponential multiplication corresponding to 2-Hz line broadening (18). The acquisition time was 205 ms and the repetition time was 3.5 s. (Glu = glutamate; Gln = glutamine; GABA = γ-amino-butyrate; Asp = aspartate; NAA = N-acetyl-aspartate).

volumes (Fig. 5) implies a T_2^* of at least 140 ms, which is close to the reported T_2 of 160 ms (24), leaving less than 0.01 ppm contribution of inhomogeneity to the linewidth. The carbon linewidths of 2 Hz imply that T_2 for carbon metabolites is above 170 ms. Linewidths in ^{1}H spectra of 36 ml volumes were typically 4 Hz and as low as ~ 3 Hz. ^{1}H spectroscopy benefitted from the close to Lorentzian lineshapes (Fig. 6C) and from the significantly improved water suppression, which is essential for quantitative *in vivo* ^{1}H NMR spectroscopy at these field strengths.

The time requirements for FASTMAP can be cut to 30s by halving the number of repeat cycles (presently 2) and by improved computer speed. The time required for the extraction of the shim correction currents was prolonged due to the requirement to write data to disk and due to the slow performance of the floating point arithmetic of the spectrometer computer. Calculation time can be reduced to a few seconds when using contemporary hardware.

The FASTMAP procedure explicitly uses the formalism of spherical harmonics to analyze the inhomogeneity and to characterize the shim coil fields. However, the application of the method is not restricted to situations where the field generated by any shim coil corresponds to a single spherical harmonic, since the former can always be described as a linear combination of spherical harmonic functions (14). In fact, the calibrations presented in columns 4 and 5 of Table 1 suggest that the field generated by most shim coils is adequately described by the corresponding associated spherical harmonic function.

The precision of FASTMAP can be improved as suggested from the noise error calculations presented in Eqs. [7] and [8]. First, it is noted that the rms deviations of the linear and quadratic polynomial coefficients, σ_1 and σ_2,

respectively, are inversely proportional to the signal-to-noise ratio M/σ of the projection. It is in principle possible to raise M/σ by a factor 2 by replacing the stimulated-echo sequence in Fig. 1 with a Hahn spin-echo using slice-selective 90° and 180° pulses to define the bar's orientation, with equal sensitivity to B_1 variations. It is, however, necessary to ensure that eddy-current-effects are not significant during the extra-delay between the two pulses. M/σ can be additionally improved by increasing the voxel size along the projections either by increasing the cross-sectional area A, or by increasing Δr. However, it should be noted that a certain length-to-width ratio $L/A^{1/2}$ needs be maintained to ensure that the phase is mainly determined by variations along the bar, not across. In practice, a ratio $L/A^{1/2}$ of approximately 3 seemed sufficient. Second, it is noted that the polynomial coefficients a_1 and a_2 are best determined when the selected bar length L is maximal, as can be seen from the expressions in Eq. [8]. The maximization of L is however limited by the organ dimensions and the increased probability of significant contributions from third- and higher-order terms ($n \geq 3$) to the inhomogeneity present in the volume. The method will be most efficient at high fields as inferred from the decreased σ_{ppm} in Eq. [7] due to increases in the signal-to-noise M/σ and the Hz-to-ppm conversion factor ν_0.

Other techniques potentially capable of localized, automatic shimming with second-order shim coils have been recently described (8–12), all of which rely in one form or another on the acquisition of image data sets with concomitant increases in measurement and computational time. For instance, the adjustment of *all* linear and *all* quadratic coils requires the acquisition of at least *six* two-dimensional images. On the other hand, only 12 projections are needed with FASTMAP. Spectroscopic imaging of the water signal results in long measuring times that are prohibitive for *in vivo* application (8, 9). Imaging of phase differences has therefore become the more standard method to encode the magnetic field information, enabling adjustment times as low as 10 min (10–12). All of the latter methods, however, encoded the homogeneity information after gradients are switched in the pulse sequence, which bears the risk of suboptimal adjustments due to eddy current effects. Consequently, the extra-delay τ has been kept at ~4 ms (11, 12), which is not an optimal choice for the human brain, as can be seen from Eq. [7] and Fig. 3 (T_2^*~70 ms in gray matter results in x~0.06). Using linear projections in conjunction with one-dimensional methods for phase unwrapping has the advantage of allowing long phase encoding delays (30–70 ms), resulting in a substantially improved precision. The phase unwrapping algorithm that has been used here tests for π phase jumps in the field map, which is mathematically equivalent to testing for outliers in the derivative map (11). The analysis, however, is preferably done in the original field map due to the considerably better precision, as shown at the end of the Appendix.

CONCLUSION

The automatic method adjusts all first- and second-order shim coils within 2 min in its current implementation. Considering the excellent spectral resolution achieved in ^1H, ^{31}P, and ^{13}C spectra and that the time requirements can potentially be reduced to ~30 s, this technique substantially reduces set-up time for many NMR experiments. The method's robustness with respect to eddy-currents allows its implementation on virtually any system capable of imaging.

ACKNOWLEDGMENTS

Many thanks to Terry Nixon for many fruitful discussions and for improvements and maintenance of the spectrometer, to Marcel Müri (Spectrospin AG, Fällanden, Switzerland) for providing the SCM programming guidelines, to the Cambridge group (L. D. Hall, A. Carpenter) for the gradient waveform memory programming code. Help from Doug Rothman, Calum Avison, Rusty Novotny, and Susan Boulware with the *in vivo* measurements is greatly appreciated.

APPENDIX

Derivation of Eq. [7]

The calculations are demonstrated for one phase value, i.e., the indices i and (j) are omitted and $z_{2i}^{(j)}$, $z_{1i}^{(j)}$ are now $z_2 = x_2 + iy_2$ and $z_1 = x_1 + iy_1$, respectively. Starting with the explicit form of Eq. [3],

$$\Delta\varphi = \text{atan}\left(\frac{x_1x_2 + y_1y_2}{x_1y_2 - x_2y_1}\right), \qquad [A1]$$

the expression

$$\delta(\Delta\varphi) = \frac{\partial\Delta\varphi}{\partial x_1}\delta x_1 + \frac{\partial\Delta\varphi}{\partial y_1}\delta y_1 + \ldots \qquad [A2]$$

is calculated, which results after a lengthy calculation in the rearranged expression

$$\delta(\Delta\varphi) = \frac{x_1\delta y_1 - y_1\delta x_1}{x_1^2 + y_1^2} + \frac{y_2\delta x_2 - x_2\delta y_2}{x_2^2 + y_2^2}. \qquad [A3]$$

Eq. [A3] is identical to the corresponding expression obtained from the conventional method of calculating the phase difference, i.e., $\Delta\varphi = \arg(z_2) - \arg(z_1)$.

Assuming uncorrelated noise of equal rms amplitude σ in x_1, x_2, y_1, and y_2, and setting $\sigma^2(\Delta\varphi)$ to the expectation value of $(\delta(\Delta\varphi))^2$, we obtain

$$\sigma^2(\Delta\varphi) = \sigma^2\left(\frac{1}{x_1^2 + y_1^2} + \frac{1}{x_2^2 + y_2^2}\right). \qquad [A4]$$

Applying the scaling from Eq. [4] with the definitions $x_1^2 + y_1^2 = M^2$, $x_2^2 + y_2^2 = M^2e^{-2x}$ and $\sigma(\Delta\varphi) = \sigma_{ppm}$ leads to Eq. [7] ($x = \tau/T_2^*$).

Derivation of Eq. [8]

The linear coefficient a_1 (Eq. [5]) was calculated within $\pm L/2$, using the standard equation

$$a_1 = \frac{\sum r_i\Delta\nu_i}{\sum r_i^2}. \qquad [A5]$$

By calculating the partial derivative with respect to $\Delta\nu_i$ analogous to the first part of the Appendix and by setting

the rms amplitude of the noise in $\Delta\nu_i$ to σ_{ppm}, we obtain

$$\sigma_1 = \sigma(a_1) = \sigma_{ppm} (\sum r_i^2)^{-1/2} \quad [A6]$$

From the expression for a_2 evaluated within $\pm L/2$ according to

$$a_2 = \frac{\sum r_i^2 \sum \Delta\nu_i - N \sum r_i^2 \Delta\nu_i}{(\sum r_i^2)^2 - N \sum r^4}, \quad [A7]$$

$\sigma_2 = \sigma(a_2)$ is obtained in an analogous manner:

$$\sigma_2 = \sigma_{ppm} [\sum r_i^4 - N^{-1} (\sum r_i^2)^2]^{-1/2}. \quad [A8]$$

With a sufficiently fine digitization $\Sigma r_i{}^n$ in Eqs. [A6] and [A8] can be expressed by the integral from $-L/2$ to $+L/2$,

$$\sum r_i^n \simeq \frac{1}{\Delta r} \int_{-L/2}^{+L/2} r^n dr = \frac{1}{\Delta r} \frac{1}{n+1} \frac{L^{n+1}}{2^n} \quad [A9]$$

Using Eq. [A9] combined with Eq. [A6] results in σ_1 given in Eq. [8], and combining Eq. [A9] and Eq. [A8] with $n = L/\Delta r$ gives σ_2 in Eq. [8].

If a_1 is calculated from the derivative of $\Delta\nu$, i.e., $\Delta\nu^* = \Delta\nu/\Delta r$ (11), this amounts to a lowered precision, since now $a_1 = a_0{}^*/\Delta r$ and $a_2 = a_1{}^*/\Delta r$, and the corresponding $\sigma_1{}^* = \sigma_{ppm} L^{-1/2} \Delta r^{1/2} 2^{1/2} \Delta r^{-1}$ and $\sigma_2{}^* = \sigma_{ppm} L^{-3/2} \Delta r^{1/2} 2^{1/2} \Delta r^{-1} C_1$ are larger than σ_1 and σ_2 in Eq. [8] for a given σ_{ppm}.

REFERENCES

1. T. R. Brown, B. M. Kincaid, K. Ugurbil, *Proc. Natl. Acad. Sci. USA* **79,** 3532 (1982).
2. W. T. Dixon, *Radiology* **153,** 189 (1984).
3. A. M. Blamire, G. McCarthy, R. Gruetter, D. L. Rothman, Z. Rattner, F. Hyder, R. G. Shulman, 11th Annual Meeting, Soc. Magn. Reson. Med., Abstract 1834, Berlin, August 8–14, 1992.
4. D. Holz, D. Jensen, R. Proks, M. Tochtrop, W. Vollmann, *Med. Phys.* **15,** 898 (1988).
5. D. M. Doddrell, G. J. Galloway, I. M. Brereton, W. M. Brooks, *Magn. Reson. Med.* **7,** 352 (1988).
6. P. C. M. van Zijl, C. T. W. Moonen, J. R. Alger, J. S. Cohen, S. A. Chesnick, *Magn. Reson. Med.* **10,** 256 (1989).
7. D. I. Hoult, *J. Magn. Reson.* **73,** 174 (1987).
8. J. Wilkins, S. Miller, *IEEE Trans. Biomed. Eng.* **36,** 202 (1989).
9. J. Tropp, K. A. Derby, C. Hawrysko, S. Sugiura, H. Yamagata, *J. Magn. Reson.* **85,** 244 (1989).
10. M. G. Prammer, J. C. Haselgrove, M. Shinnar, J. S. Leigh, *J. Magn. Reson.* **77,** 40 (1988).
11. E. Schneider, G. Glover, *Magn. Reson. Med.* **18,** 335 (1991).
12. P. Webb, A. Macovsky, *Magn. Reson. Med.* **20,** 113 (1991).
13. R. Gruetter, C. Boesch, *J. Magn. Reson.* **96,** 323 (1992).
14. F. Romeo, D. I. Hoult, *Magn. Reson. Med.* **1,** 44 (1984).
15. R. Gruetter, E. J. Novotny, S. D. Boulware, D. L. Rothman, G. F. Mason, G. I. Shulman, R. G. Shulman, W. V. Tamborlane, *Proc. Natl. Acad. Sci. USA* **89,** 1109 (1992).
16. R. Gruetter, D. L. Rothman, E. J. Novotny, R. G. Shulman, *Magn. Reson. Med.* **25,** 204 (1992).
17. R. Gruetter, D. L. Rothman, E. J. Novotny, G. I. Shulman, J. W. Prichard, R. G. Shulman, *Magn. Reson. Med.* **27,** 183 (1992).
18. R. Gruetter, E. J. Novotny, S. D. Boulware, D. L. Rothman, W. V. Tamborlane, R. G. Shulman, 11th Annual Meeting, Soc. Magn. Reson. Med., Abstract 1921, Berlin, August 8–14, 1992
19. E. J. Novotny, R. Gruetter, S. D. Boulware, D. L. Rothman, R. G. Shulman, 11th Annual Meeting, Soc. Magn. Reson. Med., Works-in-Progress, Abstract 1961, Berlin, August 8–14, 1992
20. P. R. Luyten, G. Bruntink, F. M. Stoff, J. W. A. H. Vermeulen, J. I. van der Heyden, J. A. den Hollander, A. Heerschap, *NMR Biomed.* **1,** 177 (1989).
21. R. J. Ordidge, A. Connelly, J. A. B. Lohman *J. Magn. Reson.* **66,** 283 (1986).
22. R. Gruetter, D. L. Rothman, E. J. Novotny R. G. Shulman, 11th Annual Meeting, Soc. Magn. Reson. Med., Abstract 3808, Berlin, August 8–14, 1992
23. W. H. Press, B. P. Flannery, S. A. Teukolsky, W. T. Vetterling, "Numerical Recipes in Pascal." Cambridge University Press, Cambridge, UK, 1989.
24. K. D. Merboldt, D. Chien, W. Hänicke, M. L. Gyngell, H. Bruhn, J. Frahm, *J. Magn. Reson.* **89,** 343 (1990).